Mapping Time-Dependent Conductivity of Metallic Nanowire Networks by Electrical Resistance Tomography toward Transparent Conductive Materials

(Article begins on next page)

29 November 2021

Mapping Time-dependent Conductivity of Metallic Nanowire Networks by Electrical Resistance Tomography toward Transparent Conductive Materials

Gianluca Milano[1,2], Alessandro Cultrera[3], Katarzyna Bejtka[4], Natascia De Leo[1], Luca Callegaro[3], Carlo Ricciardi[2*] and Luca Boarino[1]*

[1]Advanced Materials Metrology and Life Sciences Division, INRiM (Istituto Nazionale di Ricerca Metrologica), Strada delle Cacce 91, 10135 Torino, Italy.

[2]Department of Applied Science and Technology, Politecnico di Torino, C.so Duca degli Abruzzi 24, 10129 Torino, Italy.

[3]Quantum Metrology and Nanotechnologies Division, INRiM (Istituto Nazionale di Ricerca Metrologica), Strada delle Cacce 91, 10135 Torino, Italy.

[4]Center for Sustainable Future Technologies, Istituto Italiano di Tecnologia, Via Livorno 60, 10144 Torino, Italy.

KEYWORDS

ABSTRACT

Metallic nanowire (NW) networks have attracted great attention as promising transparent conductive materials thanks to the low sheet resistance, high transparency, low cost production and compatibility with flexible substrates. Despite many efforts have been devoted to investigating the conduction mechanism, a quantitative characterization of local electrical properties of nanowire networks at the macroscale still represents a challenge. In this work, we report on the investigation of local electrical properties and their evolution over time of Ag NW networks by means of electrical resistance tomography (ERT). Spatial correlation of local conductivity properties and optical transparency revealed that the non-scanning and rapid ERT technique allows to probe local electrical inhomogeneities in the NW network, differently from conventional measurement techniques such as van der Pauw and four-point probe. In addition, ERT mapping over time was employed for *in situ* monitoring the evolution of Ag NW networks conductivity, elucidating the dependence of the degradation of local electrical properties under ambient exposure on the initial conductivity. Our results shed light on the importance of the characterization of local electrical properties of NW networks where uniformity and stability represent the main challenges to overcome for their use as transparent conductive materials.

INTRODUCTION

Metallic nanowire (NW) networks combining high electrical conductivity, high transparency, high flexibility and stretchability are considered emerging candidates as transparent conductive materials (TCMs), being particularly promising for cost-effective replacement of indium tin oxide (ITO) thanks to the compatibility with solution-based processing, large area deposition techniques and high throughput production.[1–10] Due to these characteristics, metallic NW networks realized with a bottom-up approach have been exploited for a wide range of applications including transparent electrodes (TEs) for flexible electronics[11–15], photovoltaics[16,17], film heaters[18,19], electronic textiles[20] as well as for the realization of electromagnetic and optoelectronic devices for sensors and information communications technology (ICT)[21–25]. For all these applications, the characterization of electronic conduction properties of metallic NW networks over different length scales represents a key aspect not only for unveiling the conduction mechanism but also to optimize their performances depending on the target application. Despite many efforts have been devoted to the investigation of the conduction properties of metallic NW network at the micro/nanoscale, characterization of network conductivity at the macroscale still represents a challenge. At the nanoscale, devices based on single NWs and single NW junctions have been realized to investigate electrical properties of single building blocks of the network.[26–29] Instead, NW network conduction properties at the microscale have been investigated by means of conductive atomic force microscopy (C-AFM) and voltage contrast imaging in scanning electron microscopy (SEM).[23,30] Even though these techniques can be employed to identify NWs that actively contribute to the network conductivity allowing direct investigation of current paths and making possible to correlate electrical properties with the network morphology, these methods allow to investigate conduction properties of NWs over a limited area of tens of microns. On the

other hand, electrical properties of NW networks at the macroscale are usually assessed by means of two point probe (2PP)[27,31] or four point probe (4PP) measurements[12,32,33]. These techniques allow to evaluate the overall conductivity of the NW network without providing details concerning the spatial distribution of electrical properties across the network. Understanding local electrical properties is even more important than evaluating the overall conductivity for a wide range of applications, since network inhomogeneities are related to propagation of cracks, point of failure and local overheating phenomena that limit device performances even causing device breakdown.[1,34,35] For example, Kim et al.[35] by infrared imaging reported that inhomogeneous networks with self-aggregated NW islands lead hot spots in the sample due to localized heating effects. The Joule heating problem of NW networks was analyzed by Khaligh et al.[36] that reported that the presence of local hot spots is responsible for an acceleration of NW degradation leading to electrode failure. Also, Sannicolo et al.[34] reported that local inhomogeneities can lead to a non-uniform distribution of the electric field when the NW network is biased, influencing failure dynamics during propagation of cracks. In case of NW networks integrated in solar cells, these inhomogeneities can lower device efficiency by increasing the series resistance. It is worth noticing also that, since the NW network conductivity is related to network density, local inhomogeneities of electrical properties can be correlated also to local variations of optical transparency.[37] With the aim of characterizing spatial distribution of electrical properties at the macroscale, conduction in NW networks was investigated by means of infrared thermography.[38] Despite being a promising tool for visually identify conductive channels and local hot spots, this technique fails in providing information on local NW network conductivity properties. As an alternative, Sannicolo et al.[34] reported one-probe electrical mapping (1P-mapping) by scanning a tip probe across a biased NW network to locally measure the electrical potential, allowing spatial

mapping of the voltage equipotential lines in the device and providing information about sample homogeneity. However, *i)* the time for acquiring an electrical map with one-probe technique scales with the sample area, thus limiting its scalability and *ii)* this technique fails in quantitative estimation of local conductivity across the sample. In addition, both infrared thermography and 1P-mapping necessarily require the realization of proper NW network devices involving the realization of metal electrodes. In this framework, a scalable, fast and quantitative technique to probe local conductivity properties of metallic NW networks over large area is currently missing. In this work, we report on mapping of metallic Ag NW network conductivity over large scale ($\sim cm^2$) by means of electrical resistance tomography (ERT). Differently from conventional techniques adopted for electrical characterization of NW networks, this non-scanning technique allows a quantitative and traceable to the international system of units (SI) characterization of local conduction properties of metallic networks and its evolution over time. In case of nearly uniform Ag NW network samples, ERT results are in good accordance with electrical conductivity obtained by conventional 4PP and van der Pauw (vdP) measurements. More interestingly, ERT allows to probe electrical inhomogeneities in NW networks as discussed by spatially correlating local conductivity and optical transparency. Moreover, ERT was employed to track *in situ* the spatial distribution of the network conductivity over time, showing that the degradation of local conductivity properties under ambient exposure depends on the initial conductivity distribution of the network. In particular, more pronounced variations of conductivity are correlated to sample areas characterized by lower initial conductivity. Besides showing that ERT represents a versatile technique to obtain conductivity maps, these results shed new light on the importance of characterizing local conduction properties of metallic NW networks and their evolution over time. In this framework, ERT mapping results particularly promising for the development of next-

generation transparent conductive materials and electronic devices based on metallic nanowire networks where uniformity and stability represent the most important technical challenges to overcome.

EXPERIMENTAL SECTION

NW network fabrication and characterization

Metallic NW networks were fabricated by drop casting Ag NWs with diameter of about 115 nm and length of 20-50 μm in isopropyl alcohol suspension (from Sigma-Aldrich) on a square crystal quartz (z-cut) substrate of 10×10 mm². Chemical and structural properties of Ag NWs employed in this work were analysed in our previous work.[22] Different metallic NW network densitites were obtained by diluting NWs in different volumes of isopropyl alcohol suspension. By controlling the concentration of Ag NWs in the suspension and by fixing the volume deposited on the 10×10 mm² substrate to 13.8 μl it was possible to estimate the areal mass density (AMD). The volume of suspension deposited on the substrate was optimized to obtain homogeneous distribution of NWs all over the sample. In order to obtain an intentionally nonuniform distribution of NWs over the 10×10 mm² sample, drop casting was performed by keeping the quartz substrate tilted. The normalized NW density was estimated by using the relation $D = N\frac{L^2}{S^2}$, where N is the number of NWs, L is the average NW length (35 μm) and S is the size of the 2D plane where NWs are randomly deposited.[39] Morphological characterization of the NW networks on the quartz substrate was performed by Scanning Electron Microscopy (SEM; FEI Inspect F) and by optical microscopy. Transmittance spectra of metallic NW networks in the wavelength range of 400-900 nm were acquired by means of a α-SE^TM Ellipsometer by J.A. Woollam Co., Inc. Transmittance spectra of bare NW networks were obtained by properly taking into account of the absorbance of

the bare quartz substrate. Transmission Electron Microscopy (TEM) was performed by means of a FEI Tecnai F20ST operating at 200 kV, by spotting a dispersion of Ag NWs on a TEM grid. X-ray photoelectron spectroscopy (XPS) was performed by using a Kα source with energy of 1486.6 eV and using the C 1s peak position (284.8 eV) as calibration.

ERT measurement setup and map reconstruction

Electrical measurements were performed with a setup that consists of a Keysight 34980A multifunction unit equipped with a switch matrix module (Keysight 34933 read matrix module), a Keithley 2602B source-meter and an Agilent 34461A digital multimeter. Samples were contacted with a fixture provided of spring-mounted needle probes described in a previous work.[40] The needle probes have a round tip with a contact section of about 40 μm in diameter. The probe diameter was observed to provide reliable electrical contacts in NW networks with AMD considered in our work (60 mg/m^2 – 181 mg/m^2). The distance between nearby contact needles along an edge is 2 mm while the distance between nearby contacts at the corner is 2.12 mm. The sample is preliminarily loaded in an engraved plastic support to keep it in the correct position. The support is loaded in the fixture that is provided of an actuator lever, which allows to land the probe array on the sample. The probes make physical contact to the NW network (with a mechanical force of 0.15 N) at its boundaries, at 500 μm from its edges (a schematization of the contact geometry is reported in Supporting Information S1). After that the sample is connected to the electrical measurement setup, the switch matrix defined the stimulation-measurement pattern consistently with the adjacent protocol as discussed in Supporting Information S2. The measurement accuracy was estimated by taking into account both standard deviation of repeated measurements and instrument accuracy from one-year specification given by the manufacturer.

The time evolution of Ag NW network conductivity was performed in air (relative humidity in the range of 47-56 %) at room temperature of 22 (1) °C without moving the needle probes.

The ERT image reconstruction process involves the minimization of a functional in σ:

$$\min_{\boldsymbol{\sigma}} \{\|\boldsymbol{V_m} - \boldsymbol{U}(\boldsymbol{\sigma})\|^2 + \lambda R(\boldsymbol{\sigma})\} \tag{1}$$

that includes the measured boundary voltages at sample edge $\boldsymbol{V_m}$, a set of calculated voltages $\boldsymbol{U}(\boldsymbol{\sigma})$ at electrode positions obtained from the model given a conductivity distribution over the whole sample domain and a regularization term $R(\boldsymbol{\sigma})$ introduced to counterbalance the ill-posed nature of the inverse problem. The norm $\|\boldsymbol{V_m} - \boldsymbol{U}(\boldsymbol{\sigma})\|$ represents the Euclidean distance between $\boldsymbol{V_m}$ and $\boldsymbol{U}(\boldsymbol{\sigma})$, while $\lambda R(\boldsymbol{\sigma})$ is the regularisation term, where λ is the parameter that sets the amount of regularisation. In this work we used a Tikhonov regularisation $R(\boldsymbol{\sigma}) = \|\boldsymbol{\sigma}\|^2$ [41], typically applied to ERT[42]. The value of λ was selected by means of the so-called *L*-curve method.[43] The value of λ chosen by the method is dependent on all the individual transresistance measurements performed, in turn dependent on the whole conductivity map of the specific sample. We identified a fast routine for the determination of λ that minimizes the additional computation effort required by the L-curve method.[44] It is worth noticing that the *L*-curve method allows to find the optimal balance between reconstruction error and amount of regularization (determined by λ) with an objective criterion and using only the information already included in eq. (1). No additional information other than the one included in the measurements and in the finite element model is needed to apply the *L*-curve method. The problem (1) was discretized to a finite element method (FEM) with elements reasonably dense not to affect the maps resolution. The image reconstruction algorithm that run on the FEM was based on one of the available Gauss-Newton absolute iterative solvers of the EIDORS 3.7.1 library. The problem (1) was discretized to a FEM with elements

reasonably dense not to affect the map resolution. EIDORS' routines were also used to graphically render the solution (see Supporting Information S3 for details on the image reconstruction process).

vdP, 2PP and 4PP measurement setup

The same setup and dataset of ERT measurements was exploited for applying the vdP method, by taking into account of four terminal configuration which allowed the use of a simple formulation for this technique without numerical corrections.[40] This occur when driving electrodes are placed on a line of symmetry of the sample while measuring electrodes are symmetrically located with respect to that line.[44] 2PP and 4PP measurements were performed by means of a four probe head (Jandel) with cylindrical needles with radius of 40 μm and interspacing distance of 0.635 mm connected with a source-meter (Keithley 6430).

RESULTS AND DISCUSSION

Mapping NW network conductivity at the macroscale

Metallic NW networks were realized by drop-casting Ag-NWs in suspension on a 10×10 mm^2 quartz substrate, as reported in Figure 1a and b. Details on NW dimensions and deposition technique can be found in Experimental section. The emergent electronic conduction properties of metallic NW networks at the macroscale are determined by the high number of interconnections among NWs at the nanoscale providing electronic conduction paths (Figure 1c). In this scenario, the NW network can be understood as a resistance network where the overall conductivity is determined by the NW density, the wire resistances and the junction resistances between intersecting NWs.[39,45] The measurement of the electrical properties with ERT was performed by directly contacting the metallic NW network with needle probes at the sample boundaries, as

schematized in Figure 1d. In this fashion, electrical properties of the network can be directly assessed without the need of fabricating metallic electrodes through deposition techniques (the effect of the pressure exerted by the needle probes on the NW networks are discussed in Supporting Information S4). The set of four-terminal transresistances required as input quantities for the ERT method were acquired through a dedicated measurement setup by exploiting an adjacent pattern measurement scheme where an input current is injected by imposing a voltage difference in a pair of adjacent contacts while measuring the voltage across all the remaining pairs of adjacent electrodes, as schematized in Figure 1e. Details on the dedicated measurement setup and measurement protocols can be found in the Experimental section. It is worth to underline that all measurements were performed in a four-terminal configuration in order to exclude the effect of contact resistances (the effect of contact resistance in two-terminal configuration is discussed afterwards). The adjacent measurement pattern provides a set of *n(n-3)* transresistances, where *n* = 16 is the number of electrodes. The obtained set of transresistances was employed to construct the impedance matrix that electrically represents the NW network system. An example of impedance matrix obtained by measuring transresistances across a metallic NW network sample is reported in Figure 1f. Missing elements of the matrix are related to configurations that are not measurable in four-terminal configuration and, for this reason, are disregarded since they include an unknown contact resistance. The symmetry of the impedance matrix reflects the reciprocity of the electrical network of nanowires: the same transresistance is measured if source and sense terminals are exchanged. (i.e. the same value of transresistance is observed by injecting current in electrodes 1-2 and measuring voltage drop in between electrodes 11-12 or viceversa), as for any passive electrical network in absence of an external magnetic field. The impedance matrix is then used as input for the ERT reconstruction of the conductivity map.[40,46,47] At the macroscale,

conduction properties are expected to be isotropic due to the random orientation of NWs (according to ref.[48]) and the network can be assumed as a continuous conductive medium. Indeed, despite the microscopic structure, it was shown that the approximation as a continuous conductive medium holds over a scale of a few NW length when the normalized density $D > 2D_c$, where D_c=5.63 is the normalized density at the percolation threshold.[39] In our case, this approximation is reasonable since in all the considered samples the normalized density was estimated to be $D > 25$. Also, the approximation as a continuous medium is in agreement with resistance grid network models, where the effective resistance measured in between 3 or 4 lattice spacings apart well matches with that of a continuous uniform sheet.[49] In the continuous approximation, the electrostatic problem can be described by the Laplace equation:

$$\nabla \cdot [\sigma(P)\nabla\phi(P)] = 0 \tag{2}$$

where ∇ and $\nabla \cdot$ are the gradient and divergence operators, respectively, while $\sigma(P)$ and $\phi(P)$ are the conductivity and electrostatic potential at a generic point P of the conductive surface here represented by the NW network. Obtaining a conductivity map of the sample surface requires the solution of an inverse electrostatic problem, consisting in determining the value $\sigma(P)$ for each point of the NW network given the information on $\phi(P)$ and on the current density $j(P) = -(\sigma(P)\nabla\phi(P))$ on the surface. In case of ERT, the required information is given in terms of the impedance matrix, the sample geometry and the position of electrodes as inputs. This represent an ill-posed, ill-conditioned and nonlinear problem that was solved by means of optimization techniques with numerical methods (details in the Experimental section).[40,46,47] In brief, the sample geometry and electrode positions were considered in a finite element model and conductivity maps were retrieved using a Gauss-Newton method to minimize eq. (1). The finite element solution is interpolated and then discretized on a grid of 100×100 pixels. Figure 1g reports the ERT

conductivity map of a metallic NW network obtained by taking the impedance matrix of Figure 1e as input for the numerical solver. As it can be observed, ERT allows for a spatial-resolved characterization of the local electrical properties of NW networks at the macroscale over large area. Note that the acquisition of the whole set of measurements necessary for ERT reconstruction was performed in less than 300 s with a measurement accuracy of the transresistance better than the 0.5 % (an uncertainty budget is available in Sec 2.2.3 of ref.[50]). It is worth noticing that the measurement speed can be even higher, which can be of interest depending on the final application, though at the cost of a lower accuracy. Being a non-scanning technique, an important aspect is that the measurement speed does not depend on the area under investigations. Concerning the spatial resolution of the ERT conductivity maps, it is necessary to take into account that it depends mainly on the amount of available boundary measurements and, thus, is limited by the number of contacts: features smaller that the distance in between electrodes are smeared out.[40] Thus, the spatial resolution of mapping can be further increased by increasing the number of contact electrodes. In this context, it is important to remark the effective scalability of the ERT technique that allows to map conductivity of metallic NW networks over large area by properly engineering the number of electrodes and their distance, taking into account that the inter-electrode distance have to be adjusted depending on the target spatial resolution.
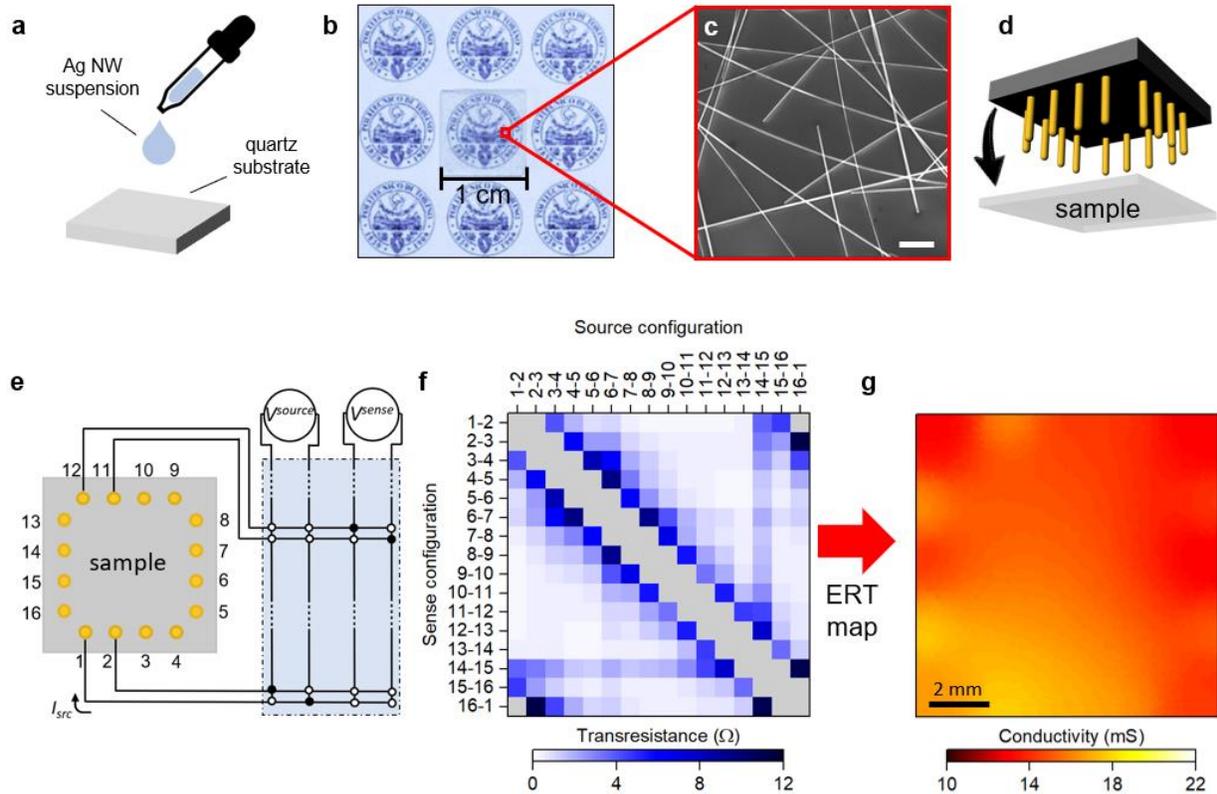
Figure 1. Experimental setup for mapping NW network conductivity at the macroscale through ERT. (a) Schematization of the fabrication of Ag NW networks deposited by drop-casting on a 10×10 mm^2 quartz substrate and (b) image of the transparent quartz substrate after NW deposition, with logo of Politecnico di Torino as background. (c) SEM image of a detail of the network morphology at the nanoscale showing highly interconnected NWs (scale bar, 2 μm). (d) Schematic representation of electrical contacts realized by landing metallic needle probes on the NW network. (e) Schematic representation of the electrical measurement setup where an input current is injected by imposing a voltage difference (V^{source}) between a pair of adjacent contacts while measuring the voltage across a different pair of adjacent electrodes (V^{sense}) to measure the transresistance value. All transresistance values were measured in a four-terminal configuration by means of a

switching unit. (f) Example of an impedance matrix that electrically represents the NW network and (g) corresponding conductivity map obtained through ERT reconstruction.

Comparison of ERT, van der Pauw and 4-point probes methods

In order to test the ERT for the reconstruction of conductivity maps of NW networks, samples of different NW densities were investigated. For this purpose, samples with an estimated areal mass density (AMD) of 60, 90 and 181 mg/m^2 were realized. Representative SEM and optical images of NW networks with different densities are reported in Figure 2 a-c and Figure 2 d-f, respectively. Conductivity maps of 10×10 mm^2 NW network samples characterized by AMD of 60, 90 and 181 mg/m^2 are reported in Figure 2 g, h and i, respectively (corresponding *L*-curves considered for selecting the regularization parameter for solving the ill-posed inverse problem for conductance map reconstruction are reported in Supporting Information S5). As expected, higher conductivity was observed in samples characterized by higher AMD. For the sake of completeness, optical transmittance properties of the measured NW networks are reported in Supporting Information S6, which was possible by taking advantage of the transparent quartz substrate (see Figure 1a). Instead, more interesting is the comparison of results on conductivity obtained by the ERT method with results obtained by conventional techniques usually adopted to probe the conductivity of NW networks, such as vdP and 4PP methods. For this purpose, the distribution of the ERT conductivity map pixels (corresponding to conductivity maps reported in Figure 2 g-i) was compared with conductivity obtained by vdP and 4PP measurements acquired on the same sample. Conductivities obtained with the vdP method were extracted through the analysis of the same dataset of four-terminal measurements employed for ERT reconstruction, while 4PP measurements were performed in arbitrary locations of the sample by means of a dedicated setup with 4 inline probes (details in the Experimental section). Note that 2PP measurements were not considered due to the

presence of non-negligible contact resistance that was observed to be dependent on the NW density (see Supporting Information S7). To show the consistency of the comparison between ERT, vdP and 4PP methods, measurements were also performed on a uniform commercial conductive glass reference sample (FTO, fluorine doped tin oxide on soda-lime glass) as reported in Supporting Information S8. Results concerning NW networks reported in Figure 3 show that the distribution of conductivity of ERT map pixels is compatible with the conductivity obtained by vdP measurements for all the sample densities while slight deviations were observed by employing the 4PP technique. Despite the good agreement with vdP and 4PP techniques corroborates the validity of ERT applied to NW networks, it is important to remark that the requirements of both vdP and 4PP methods are themselves not completely satisfied since both methods assume uniform conductivity over the sample. Furthermore, in case of 4PP, the sample is also assumed to be spatially infinite. Indeed, vdP and 4PP methods allow only assessing the global conductivity of the network, hindering any information about local electrical properties. In case of NW networks, where local variation in the NW distribution and mesh can lead to non-uniform electrical properties, conductivity values obtained by vdP and 4PP methods may fail in being representative of the electrical properties of the samples. In these cases, ERT represents a viable solution for probing spatial electrical inhomogeneities of NW networks, as discussed in the following.
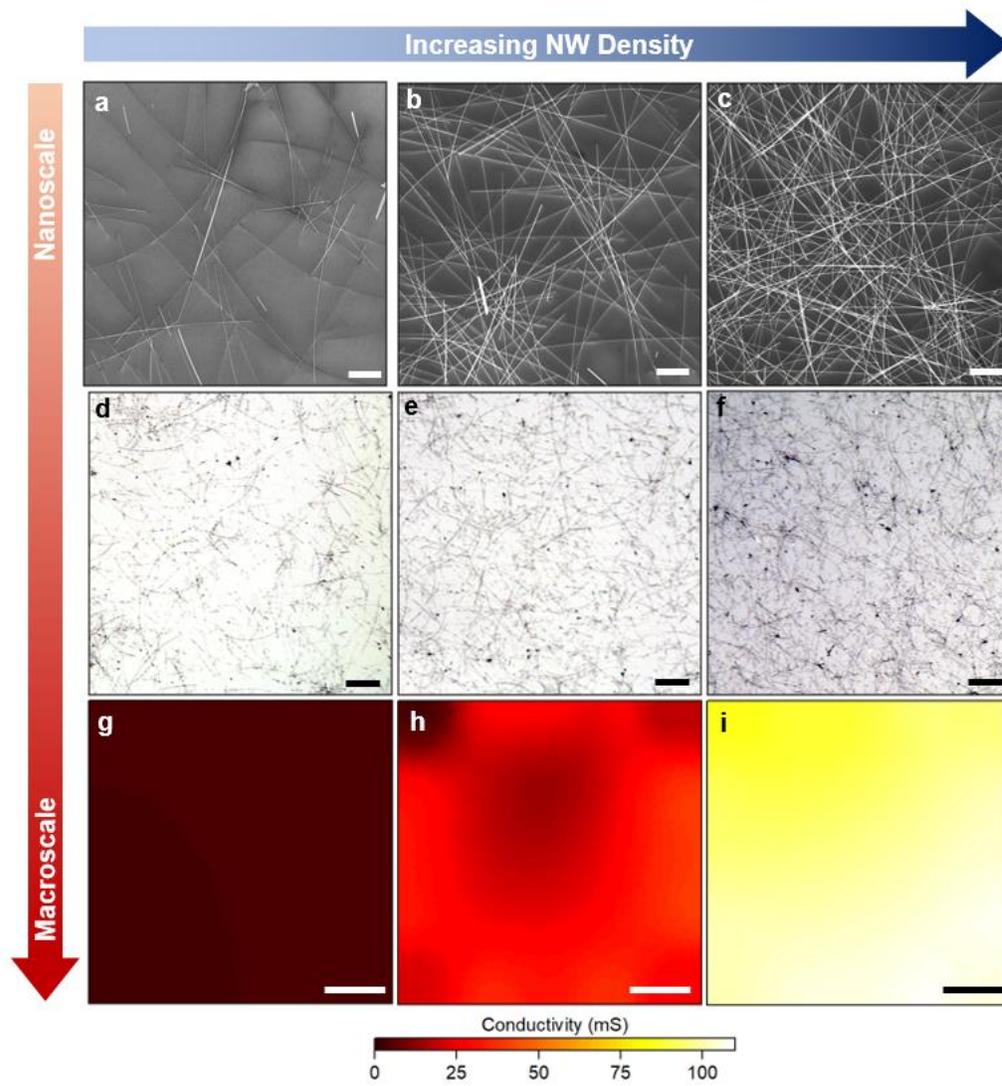
Figure 2. Conductivity maps of metallic NW networks of different densities. (a-c) Representative SEM images of NW networks (scale bar, 5 μm) and (d-f) associated optical images (scale bar, 50 μm). The estimated areal mass density was 60, 90 and 181 mg/m^2, respectively. (g-i) Conductivity maps of NW networks characterized by different densities (over a 10×10 mm^2 sample area, scale bar of 2 mm) associated with samples depicted in (a-c) and (d-f).
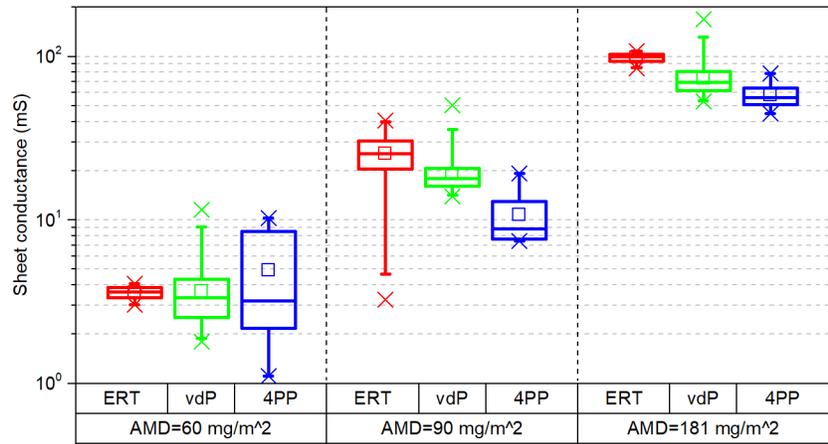
Figure 3. Comparison of ERT, vdP and 4PP methods for extraction of NW network conductivity in samples with different NW densities (AMD of 60, 90 and 181 mg/m^2). The ERT boxplots represent the distribution of conductivity pixels of the reconstructed maps (corresponding conductance maps are reported in Figure 2 g-i), the vdP boxplots represent the distribution of values obtained by considering more than 1200 different 4-terminal electrode configurations while the 4PP boxplots was obtained by measuring the conductivity with a dedicated setup in 8 random locations of the samples. Midlines represent median values, boxes the 25th and 75th percentiles, whiskers the 1st and 99th percentiles while crosses maximum and minimum values.

Probing electrical inhomogeneities

In order to demonstrate the applicability of ERT to probe electrical inhomogeneities in NW networks, an intentionally non-uniform NW network was realized by drop-casting Ag-NWs in suspension on a tilted substrate in order to obtain a gradient of the NW concentration across the sample with accumulation of NWs at one corner of the sample. As reported in Figure 4a, ERT revealed that the gradient of NW density resulted in a gradient of conductivity across the sample, with high conductivity in the upper-left angle where NWs were accumulated. In order to correlate the conductivity map to the morphological properties of the network, transmittance spectra of the Ag NW network were recorded in selected regions along the observed gradient of conductivity. Transmittance spectra acquired on the spots marked in Figure 4a are reported in Figure 4b. As it can be observed, the transmittance is larger in sample areas progressively less conductive, in accordance with a progressive decrease of NW concentration along the diagonal direction from the upper-left corner to the lower-right corner. These evidences were also corroborated by optical microscopy, as reported in Supporting Information S9. Note that, because of the electrical inhomogeneity of the sample, measurements by means of vdP and 4PP are not representative of the sample conductivity (vdP and ERT conductivities of this non-uniform sample are compared in Supporting Information S10).
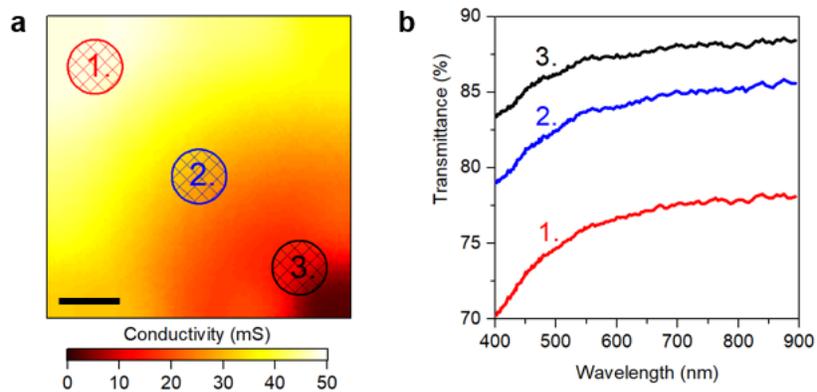
Figure 4. Probing electrical inhomogeneities in NW networks. (a) Conductivity map of a purposely non-uniform NW network realized by drop casting Ag NWs in solution on a tilted substrate causing accumulation of NWs on the upper-left corner (scale bar, 2 mm); (b) Transmittance spectra of the NW network acquired on sample areas evidenced in panel a.

Time evolution of NW network conductivity

An interesting aspect of ERT as a non-scanning technique is that it allows to investigate the evolution over time of the local electrical properties of the network. As an example, this technique can be employed to investigate the effect of degradation of local electrical properties of the metallic NW network over an extended period of time. Due to the high surface-to-volume ratio, high reactivity and poor stability related to corrosion effects were reported as main issues for integration of metallic NW networks into devices.[1,51–53] With the aim of understanding the local evolution over time, the impedance matrix describing an Ag NW network sample was repeatedly acquired every 30 minutes for about 10 days in ambient atmosphere. ERT conductivity maps corresponding to each measurement cycle unveil the time evolution of the conductivity distribution of the metallic NW network, as schematized in Figure 5a. The conductivity map of the 10×10 mm^2 sample performed at time $t = 0$ s (after NW deposition) is reported in Figure 5b. As revealed by mapping, lower conductivity was observed at the upper-left corner of the sample due to a local lower density of NWs. In order to analyze the time-dependent behavior of the local electrical properties of the network, the relative variation of average conductivity over time of the two selected areas together with the variation of the global average conductivity of the sample is reported in Figure 5c. Data are extracted from the reconstruction of 480 ERT maps acquired over more than 230 hours. At $t = 0$, the average conductivity of area (1.) and (2.) was 62 and 92 mS, respectively, while the global average of sample conductivity was 89 mS. Figure 5c shows that Ag NW networks exhibit a decrease of conductivity over time under ambient exposure. More interestingly, by observing the time-dependent behavior of conductivity in the two selected areas, it is possible to notice that the degradation process is not uniform over the sample. Indeed, stronger relative decrease of conductivity was observed in the area that was initially characterized by lower conductivity (area

1.). Here, a relative variation of almost 50 % of conductivity was observed after about 10 days while only about 15 % of variation was observed in area (2.). The average global variation of the sample conductivity was lower than 20 %. Moreover, it can be observed that the degradation process in both areas was not continuous over time but discrete steps of conductivity can be observed. Similar step-like behavior was observed also by monitoring the evolution over time of the *n(n-3)* transresistance values acquired in four-terminal configuration and two-terminal resistance measurements over time (Supporting Information S11). The step-like variation of conductivity at the macroscale results from the progressive disconnection of conductive pathways in the NW network arising from the degradation of electrical properties of NWs and NW junctions at the nanoscale, as discussed later. Our results show a correlation in between the level of degradation of the conduction properties and the initial conductivity of the network. This can be clearly observed in Figure 5d where the relative variation of conductivity $\Delta\sigma/\sigma_0$ as a function of the initial conductivity σ_0 is reported for each pixel of the conductivity map at different representative timestamps. Besides showing an increasing variation of conductivity over time in accordance to the previous discussion, it is possible to notice that larger variations of conductivity are associated to map pixels exhibiting lower initial conductivity σ_0. This is evident also by considering the map of the absolute difference in between the conductivity at selected timestamps and the initial conductivity map of the sample. Difference maps reported in Figures 5e-i show that the absolute change in conductivity is larger in the upper-left corner of the sample that was initially characterized by lower conductivity. It is worth noticing that the variation of conductivity of the network over time cannot be attributed to a variation of the contact resistance over time, since the measurement set for ERT reconstruction is acquired in four-terminal configuration as discussed before. Also, current-induced and voltage-induced degradation effects of the network are

negligible since electrical measurements were performed by applying a low voltage bias (10 mV, currents in the range of 10-50 μA) and the network was not continuously biased during time-dependent measurements. In this context, degradation of electrical properties has to be attributed to morphological and structural changes of Ag NWs due to ambient exposure.
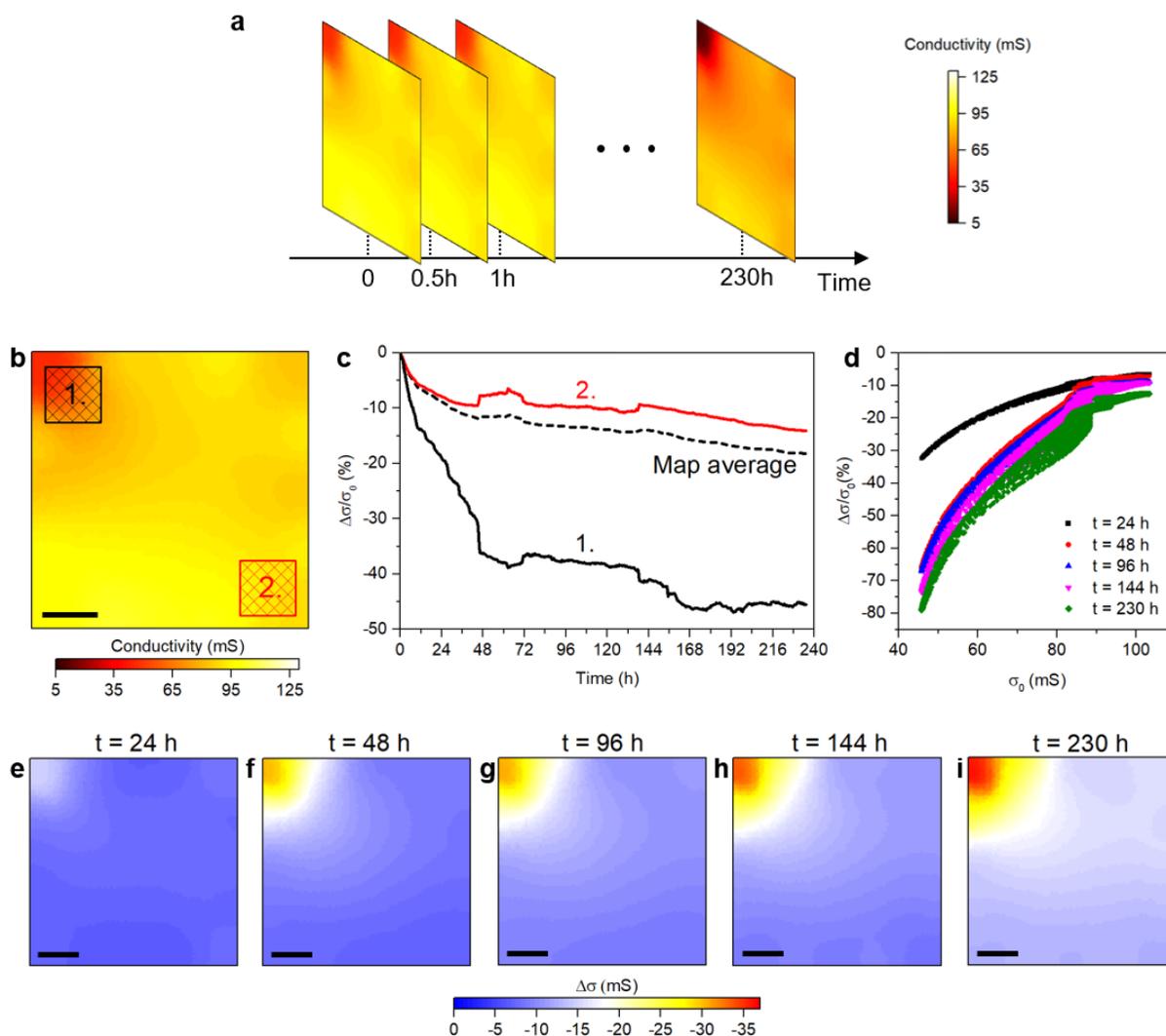
Figure 5. Time evolution of Ag NW network conductivity in ambient atmosphere. (a) Schematic representation of the time-dependent mapping of the NW network conductivity where the ERT maps were acquired by measuring the impedance matrix of the system every 30 minutes for about 10 days. (b) Conductivity map of the sample at t = 0 after NW deposition (scale bar, 2 mm). (c) Evolution of the average conductivity of areas selected in the conductivity map of panel b. The dashed line represents the time evolution of the average conductivity over the whole map. (d) Correlation in betweeen the relative variation of conductivity ($\Delta\sigma/\sigma_0$) as a function of the initial conductivity σ_0 for each pixel of the maps acquired after 24, 48, 96, 144 and 230 hours. (e-i)

Difference maps reporting the spatial distribution of the absolute change of NW network conductivity (Δσ) of maps acquired after 24, 48, 96, 144 and 230 hours (scale bars, 2 mm).

In order to investigate degradation of electrical properties at the nanoscale, morphological and structural changes in Ag NWs were monitored by transmission electron microscopy (TEM). After being exposed to air at ambient conditions for 7 days, TEM revealed the presence of silver sulfide (Ag_2S) nanoclusters on the NW surface (Figure 6 a-c) that were not initially observed after that the NW were extracted from the solution (not shown). In the electron diffraction pattern in Figure 6d reflections from Ag_2S (-112) can be identified along with the main reflections from Ag (respectively JCPDS card no. 89-3840 and 89-3722). The presence of Ag_2S after air exposure was corroborated also by chemical analysis by means of X-ray photoelectron spectroscopy (XPS) as reported in Supporting Information S12. As discussed by Elenchiguerra et al.[52], the formation of Ag_2S is driven by the presence of reduced-sulphur gases that, even if their presence in atmosphere is very low, are sufficient to initiate the corrosion process. Due to its insulating nature, the formation of Ag_2S on the NW surface is responsible for an increase of the resistance at cross-point NW junctions. Reportedly, the formation of this compound is responsible for the creation of bumps on surface and even breaks of NWs.[52] These effects at the nanoscale lead to a decrease of the conductivity of the NW network at the macroscale. The dependence of conductivity degradation at the macroscale on the initial local conductivity can be explained in terms of a different effect of corrosion depending on the NW local density. The higher degree of connectivity provided by the high number of junctions in between individual NWs in dense NW regions result in a redundancy of conducting pathways. The redundancy of conductive pathways makes high NW density regions more resistant towards the corrosion process due to fault-tolerance enhancement, since the failure

at the nanoscale of single NWs or single NW junctions is compensated by the presence of many possible alternative pathways through which the current can flow. In this context, it is important to notice that our work shed new light on the dependence of the degradation process of conductivity of NW networks on the homogeneity of the sample. This can be one of the reasons underlying the vast inconsistencies of the degradation timescales reported in literature for Ag NWs conductivity,[33,53–55] where the inhomogeneity of the samples are not taken into account since only the overall behavior of the network is analyzed. In this scenario, ERT represents an optimal tool to investigate local electrical properties of metallic NW networks and their evolution over time.
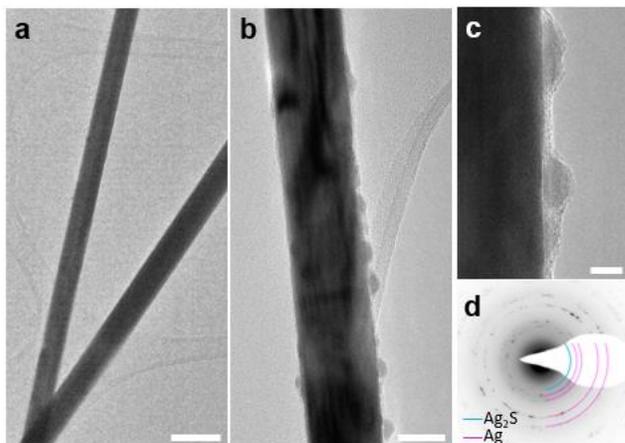

Figure 6. Ag NW morphology at the nanoscale after exposure to ambient air. (a) Bright Field TEM image of Ag NWs after exposure to ambient air for 7 days (scale bar, 200 nm). (b) TEM image acquired with higher magnification revealed the presence of amorphous Ag2S nanoclusters on the Ag NW surface (scale bar, 40 nm). (c) Detail of nanoclusters (scale bar, 10 nm) and (d) selected area diffraction (SAED) pattern confirming the presence of Ag_2S.

CONCLUSIONS

In conclusion, we investigated local electrical properties of metallic NW networks by mapping electrical conductivity through ERT over large area (~cm^2). This technique was shown to represent not only a versatile tool for mapping conductivity but also to monitor the evolution of local electrical properties over time. Besides comparing conductivity results obtained by ERT with conventional 4PP and vdP techniques in Ag NW networks, it was shown that ERT allows investigating local electrical inhomogeneities as demonstrated by spatially correlating conductivity and optical transparency. Moreover, ERT allowed *in situ* monitoring the time evolution of local electrical properties making possible to investigate the degradation of Ag NW network properties over time under ambient exposure. In particular, results revealed non homogeneous degradation of electrical properties over the sample, evidencing higher degradation in areas of the sample with initially lower conductivity. At the nanoscale, the degradation of electrical properties was observed to be related to the formation of insulating Ag$_2$S nanoclusters on the NW surface after ambient air exposure as revealed by TEM imaging. Our results evidenced that ERT represent a scalable and fast technique for spatial mapping the conductivity of metallic NW networks, making possible to probe local electrical inhomogeneities and their evolution over time. Also, in the above-mentioned scenario, ERT technique can represent a versatile tool to probe uniformity of interconnected networks for improving and optimizing the NW deposition process toward next-generation transparent conductive materials.

ASSOCIATED CONTENT

Supporting Information

The Supporting Information is available free of charge on the ACS Publication website.

Schematization of the contact geometry; details on the measurement setup and measurement protocol; detailed description of the image reconstruction process; effect of the pressure exerted by the needles on the NW networks; *L*-curves to select regularization parameter for the solution of the ill-posed inverse problem; optical transmittance properties of NW networks with different areal mass density; contact resistance dependence on the NW network density; FTO reference sample: a comparison of ERT, vdP and 4PP methods; optical characterization of nonuniform NW networks; comparison of vdP and ERT measurements on an nonuniform NW networks; time evolution of four-terminal and two-terminal measurements; XPS data;

AUTHOR INFORMATION

Corresponding Authors

Gianluca Milano: **g.milano@inrim.it**;

Carlo Ricciardi: **carlo.ricciardi@polito.it**

Notes

There are no conflicts of interest to declare.

REFERENCES

(1)   Sannicolo, T.; Lagrange, M.; Cabos, A.; Celle, C.; Simonato, J.-P.; Bellet, D. Metallic Nanowire-Based Transparent Electrodes for Next Generation Flexible Devices: A Review. *Small* **2016**, *12* (44), 6052–6075. https://doi.org/10.1002/smll.201602581.

(2)   Guo, C. F.; Ren, Z. Flexible Transparent Conductors Based on Metal Nanowire Networks. *Mater. Today* **2015**, *18* (3), 143–154. https://doi.org/10.1016/j.mattod.2014.08.018.

(3)   Ye, S.; Rathmell, A. R.; Chen, Z.; Stewart, I. E.; Wiley, B. J. Metal Nanowire Networks: The Next Generation of Transparent Conductors. *Adv. Mater.* **2014**, *26* (39), 6670–6687. https://doi.org/10.1002/adma.201402710.

(4)   Ellmer, K. Past Achievements and Future Challenges in the Development of Optically Transparent Electrodes. *Nat. Photonics* **2012**, *6* (12), 809–817. https://doi.org/10.1038/nphoton.2012.282.

(5)   Hecht, D. S.; Hu, L.; Irvin, G. Emerging Transparent Electrodes Based on Thin Films of Carbon Nanotubes, Graphene, and Metallic Nanostructures. *Adv. Mater.* **2011**, *23* (13), 1482–1513. https://doi.org/10.1002/adma.201003188.

(6)   Hu, L.; Kim, H. S.; Lee, J.-Y.; Peumans, P.; Cui, Y. Scalable Coating and Properties of Transparent, Flexible, Silver Nanowire Electrodes. *ACS Nano* **2010**, *4* (5), 2955–2963. https://doi.org/10.1021/nn1005232.

(7)   De, S.; Higgins, T. M.; Lyons, P. E.; Doherty, E. M.; Nirmalraj, P. N.; Blau, W. J.; Boland,
        J. J.; Coleman, J. N. Silver Nanowire Networks as Flexible, Transparent, Conducting Films:
        Extremely High DC to Optical Conductivity Ratios. *ACS Nano* **2009**, *3* (7), 1767–1774.
        https://doi.org/10.1021/nn900348c.

(8)   Niu, Z.; Cui, F.; Kuttner, E.; Xie, C.; Chen, H.; Sun, Y.; Dehestani, A.; Schierle-Arndt, K.;
        Yang, P. Synthesis of Silver Nanowires with Reduced Diameters Using Benzoin-Derived
        Radicals to Make Transparent Conductors with High Transparency and Low Haze. *Nano
        Lett.* **2018**, *18* (8), 5329–5334. https://doi.org/10.1021/acs.nanolett.8b02479.

(9)   Ge, Y.; Duan, X.; Zhang, M.; Mei, L.; Hu, J.; Hu, W.; Duan, X. Direct Room Temperature
        Welding and Chemical Protection of Silver Nanowire Thin Films for High Performance
        Transparent Conductors. *J. Am. Chem. Soc.* **2018**, *140* (1), 193–199.
        https://doi.org/10.1021/jacs.7b07851.

(10)   Papanastasiou, D. T.; Schultheiss, A.; Muñoz-Rojas, D.; Celle, C.; Carella, A.; Simonato,
        J.-P.; Bellet, D. Transparent Heaters: A Review. *Adv. Funct. Mater.* **2020**, *1910225*,
        1910225. https://doi.org/10.1002/adfm.201910225.

(11)   Won, P.; Park, J. J.; Lee, T.; Ha, I.; Han, S.; Choi, M.; Lee, J.; Hong, S.; Cho, K.-J.; Ko, S.
        H. Stretchable and Transparent Kirigami Conductor of Nanowire Percolation Network for
        Electronic   Skin   Applications.   *Nano   Lett.*   **2019**,   *19*   (9),   6087–6096.
        https://doi.org/10.1021/acs.nanolett.9b02014.

(12)   Cho, S.; Kang, S.; Pandya, A.; Shanker, R.; Khan, Z.; Lee, Y.; Park, J.; Craig, S. L.; Ko, H.
        Large-Area Cross-Aligned Silver Nanowire Electrodes for Flexible, Transparent, and
        Force-Sensitive Mechanochromic Touch Screens. *ACS Nano* **2017**, *11* (4), 4346–4357.
        https://doi.org/10.1021/acsnano.7b01714.

(13) Ke, S.; Guo, P.; Pang, C.; Tian, B.; Luo, C.; Zhu, H.; Wu, W. Screen-Printed Flexible Strain Sensors with Ag Nanowires for Intelligent and Tamper-Evident Packaging Applications. *Adv. Mater. Technol.* **2020**, *5* (5), 1901097. https://doi.org/10.1002/admt.201901097.

(14) Duan, S.; Wang, Z.; Zhang, L.; Liu, J.; Li, C. A Highly Stretchable, Sensitive, and Transparent Strain Sensor Based on Binary Hybrid Network Consisting of Hierarchical Multiscale Metal Nanowires. *Adv. Mater. Technol.* **2018**, *3* (6), 1800020. https://doi.org/10.1002/admt.201800020.

(15) Hosseinzadeh Khaligh, H.; Liew, K.; Han, Y.; Abukhdeir, N. M.; Goldthorpe, I. A. Silver Nanowire Transparent Electrodes for Liquid Crystal-Based Smart Windows. *Sol. Energy Mater. Sol. Cells* **2015**, *132*, 337–341. https://doi.org/10.1016/j.solmat.2014.09.006.

(16) Sun, Y.; Chang, M.; Meng, L.; Wan, X.; Gao, H.; Zhang, Y.; Zhao, K.; Sun, Z.; Li, C.; Liu, S.; Wang, H.; Liang, J.; Chen, Y.; Flexible Organic Photovoltaics Based on Water-Processed Silver Nanowire Electrodes. *Nat. Electron.* **2019**, *2* (11), 513–520. https://doi.org/10.1038/s41928-019-0315-1.

(17) Guo, F.; Azimi, H.; Hou, Y.; Przybilla, T.; Hu, M.; Bronnbauer, C.; Langner, S.; Spiecker, E.; Forberich, K.; Brabec, C. J. High-Performance Semitransparent Perovskite Solar Cells with Solution-Processed Silver Nanowires as Top Electrodes. *Nanoscale* **2015**, *7* (5), 1642–1649. https://doi.org/10.1039/C4NR06033D.

(18) Hong, S.; Lee, H.; Lee, J.; Kwon, J.; Han, S.; Suh, Y. D.; Cho, H.; Shin, J.; Yeo, J.; Ko, S. H. Highly Stretchable and Transparent Metal Nanowire Heater for Wearable Electronics Applications. *Adv. Mater.* **2015**, *27* (32), 4744–4751. https://doi.org/10.1002/adma.201500917.

(19) Sorel, S.; Bellet, D.; Coleman, J. N. Relationship between Material Properties and

Transparent Heater Performance for Both Bulk-like and Percolative Nanostructured Networks. *ACS Nano* **2014**, *8* (5), 4805–4814. https://doi.org/10.1021/nn500692d.

(20)   Atwa, Y.; Maheshwari, N.; Goldthorpe, I. A. Silver Nanowire Coated Threads for Electrically Conductive Textiles. *J. Mater. Chem. C* **2015**, *3* (16), 3908–3912. https://doi.org/10.1039/C5TC00380F.

(21)   Milano, G.; Porro, S.; Valov, I.; Ricciardi, C. Recent Developments and Perspectives for Memristive Devices Based on Metal Oxide Nanowires. *Adv. Electron. Mater.* **2019**, *5* (9), 1800909. https://doi.org/10.1002/aelm.201800909.

(22)   Milano, G.; Pedretti, G.; Fretto, M.; Boarino, L.; Benfenati, F.; Ielmini, D.; Valov, I.; Ricciardi, C. Brain-Inspired Structural Plasticity through Reweighting and Rewiring in Multi-Terminal Self-Organizing Memristive Nanowire Networks. *Adv. Intell. Syst.* **2020**, 2000096. https://doi.org/10.1002/aisy.202000096.

(23)   Manning, H. G.; Niosi, F.; da Rocha, C. G.; Bellew, A. T.; O'Callaghan, C.; Biswas, S.; Flowers, P. F.; Wiley, B. J.; Holmes, J. D.; Ferreira, M. S.; Boland, J.J.; Emergence of Winner-Takes-All Connectivity Paths in Random Nanowire Networks. *Nat. Commun.* **2018**, *9* (1), 3219. https://doi.org/10.1038/s41467-018-05517-6.

(24)   Amjadi, M.; Pichitpajongkit, A.; Lee, S.; Ryu, S.; Park, I. Highly Stretchable and Sensitive Strain Sensor Based on Silver Nanowire–Elastomer Nanocomposite. *ACS Nano* **2014**, *8* (5), 5154–5163. https://doi.org/10.1021/nn501204t.

(25)   Kim, S.-R.; Kim, J.-H.; Park, J.-W. Wearable and Transparent Capacitive Strain Sensor with High Sensitivity Based on Patterned Ag Nanowire Networks. *ACS Appl. Mater. Interfaces* **2017**, *9* (31), 26407–26416. https://doi.org/10.1021/acsami.7b06474.

(26)   Bellew, A. T.; Manning, H. G.; Gomes da Rocha, C.; Ferreira, M. S.; Boland, J. J.

Resistance of Single Ag Nanowire Junctions and Their Role in the Conductivity of Nanowire Networks. *ACS Nano* **2015**, *9* (11), 11422–11429. https://doi.org/10.1021/acsnano.5b05469.

(27)   Song, T.-B.; Chen, Y.; Chung, C.-H.; Yang, Y. (Michael); Bob, B.; Duan, H.-S.; Li, G.; Tu, K.-N.; Huang, Y.; Yang, Y. Nanoscale Joule Heating and Electromigration Enhanced Ripening of Silver Nanowire Contacts. *ACS Nano* **2014**, *8* (3), 2804–2811. https://doi.org/10.1021/nn4065567.

(28)   Selzer, F.; Floresca, C.; Kneppe, D.; Bormann, L.; Sachse, C.; Weiß, N.; Eychmüller, A.; Amassian, A.; Müller-Meskamp, L.; Leo, K. Electrical Limit of Silver Nanowire Electrodes: Direct Measurement of the Nanowire Junction Resistance. *Appl. Phys. Lett.* **2016**, *108* (16), 163302. https://doi.org/10.1063/1.4947285.

(29)   Kang, H.; Song, S.-J.; Sul, Y. E.; An, B.-S.; Yin, Z.; Choi, Y.; Pu, L.; Yang, C.-W.; Kim, Y. S.; Cho, S. M.; Kim, J.G.; Cho, J,H; Epitaxial-Growth-Induced Junction Welding of Silver Nanowire Network Electrodes. *ACS Nano* **2018**, *12* (5), 4894–4902. https://doi.org/10.1021/acsnano.8b01900.

(30)   Nirmalraj, P. N.; Bellew, A. T.; Bell, A. P.; Fairfield, J. A.; McCarthy, E. K.; O'Kelly, C.; Pereira, L. F. C.; Sorel, S.; Morosan, D.; Coleman, J. N.; Ferreira, M.S.; Boland, J.J.; Manipulating Connectivity and Electrical Conductivity in Metallic Nanowire Networks. *Nano Lett.* **2012**, *12* (11), 5966–5971. https://doi.org/10.1021/nl303416h.

(31)   Langley, D. P.; Lagrange, M.; Giusti, G.; Jiménez, C.; Bréchet, Y.; Nguyen, N. D.; Bellet, D. Metallic Nanowire Networks: Effects of Thermal Annealing on Electrical Resistance. *Nanoscale* **2014**, *6* (22), 13535–13543. https://doi.org/10.1039/C4NR04151H.

(32)   Zhu, Y.; Deng, Y.; Yi, P.; Peng, L.; Lai, X.; Lin, Z. Flexible Transparent Electrodes Based

on Silver Nanowires: Material Synthesis, Fabrication, Performance, and Applications. *Adv. Mater. Technol.* **2019**, *4* (10), 1900413. https://doi.org/10.1002/admt.201900413.

(33) Mayousse, C.; Celle, C.; Fraczkiewicz, A.; Simonato, J.-P. Stability of Silver Nanowire Based Electrodes under Environmental and Electrical Stresses. *Nanoscale* **2015**, *7* (5), 2107–2115. https://doi.org/10.1039/C4NR06783E.

(34) Sannicolo, T.; Charvin, N.; Flandin, L.; Kraus, S.; Papanastasiou, D. T.; Celle, C.; Simonato, J.-P.; Muñoz-Rojas, D.; Jiménez, C.; Bellet, D. Electrical Mapping of Silver Nanowire Networks: A Versatile Tool for Imaging Network Homogeneity and Degradation Dynamics during Failure. *ACS Nano* **2018**, *12* (5), 4648–4659. https://doi.org/10.1021/acsnano.8b01242.

(35) Kim, T.; Kim, Y. W.; Lee, H. S.; Kim, H.; Yang, W. S.; Suh, K. S. Uniformly Interconnected Silver-Nanowire Networks for Transparent Film Heaters. *Adv. Funct. Mater.* **2013**, *23* (10), 1250–1255. https://doi.org/10.1002/adfm.201202013.

(36) Khaligh, H. H.; Xu, L.; Khosropour, A.; Madeira, A.; Romano, M.; Pradére, C.; Tréguer-Delapierre, M.; Servant, L.; Pope, M. A.; Goldthorpe, I. A. The Joule Heating Problem in Silver Nanowire Transparent Electrodes. *Nanotechnology* **2017**, *28* (42), 425703. https://doi.org/10.1088/1361-6528/aa7f34.

(37) Manning, H. G.; da Rocha, C. G.; Callaghan, C. O.; Ferreira, M. S.; Boland, J. J. The Electro-Optical Performance of Silver Nanowire Networks. *Sci. Rep.* **2019**, *9* (1), 11550. https://doi.org/10.1038/s41598-019-47777-2.

(38) Sannicolo, T.; Muñoz-Rojas, D.; Nguyen, N. D.; Moreau, S.; Celle, C.; Simonato, J.-P.; Bréchet, Y.; Bellet, D. Direct Imaging of the Onset of Electrical Conduction in Silver Nanowire Networks by Infrared Thermography: Evidence of Geometrical Quantized

Percolation. *Nano Lett.* **2016**, *16* (11), 7046–7053. https://doi.org/10.1021/acs.nanolett.6b03270.

(39) Forró, C.; Demkó, L.; Weydert, S.; Vörös, J.; Tybrandt, K. Predictive Model for the Electrical Transport within Nanowire Networks. *ACS Nano* **2018**, *12* (11), 11080–11087. https://doi.org/10.1021/acsnano.8b05406.

(40) Cultrera, A.; Serazio, D.; Zurutuza, A.; Centeno, A.; Txoperena, O.; Etayo, D.; Cordon, A.; Redo-Sanchez, A.; Arnedo, I.; Ortolano, M.; Callegaro, L.; Mapping the Conductivity of Graphene with Electrical Resistance Tomography. *Sci. Rep.* **2019**, *9* (1), 10655. https://doi.org/10.1038/s41598-019-46713-8.

(41) Tikhonov, A. N.; Goncharsky, A. V.; Stepanov, V. V.; Yagola, A. G. *Numerical Methods for the Solution of Ill-Posed Problems*; Springer Netherlands: Dordrecht, 1995. https://doi.org/10.1007/978-94-015-8480-7.

(42) Vauhkonen, M.; Vadasz, D.; Karjalainen, P. A.; Somersalo, E.; Kaipio, J. P. Tikhonov Regularization and Prior Information in Electrical Impedance Tomography. *IEEE Trans. Med. Imaging* **1998**, *17* (2), 285–293. https://doi.org/10.1109/42.700740.

(43) Hansen, P. C. Analysis of Discrete Ill-Posed Problems by Means of the L-Curve. *SIAM Rev.* **1992**, *34* (4), 561–580. https://doi.org/10.1137/1034115.

(44) Cultrera, A.; Callegaro, L. A Simple Algorithm to Find the L-Curve Corner in the Regularisation of Ill-Posed Inverse Problems. *IOP SciNotes* **2020**, *1* (2), 025004. https://doi.org/10.1088/2633-1357/abad0d.

(45) Gomes da Rocha, C.; Manning, H. G.; O'Callaghan, C.; Ritter, C.; Bellew, A. T.; Boland, J. J.; Ferreira, M. S. Ultimate Conductivity Performance in Metallic Nanowire Networks. *Nanoscale* **2015**, *7* (30), 13011–13016. https://doi.org/10.1039/C5NR03905C.

(46)   Cultrera, A.; Callegaro, L. Electrical Resistance Tomography of Conductive Thin Films. *IEEE Trans. Instrum. Meas.* **2016**, *65* (9), 2101–2107. https://doi.org/10.1109/TIM.2016.2570127.

(47)   Cultrera, A.; Callegaro, L. Electrical Resistance Tomography on Thin Films: Sharp Conductive Profiles. In *2015 IEEE 1st International Forum on Research and Technologies for Society and Industry Leveraging a better tomorrow (RTSI)*; IEEE, 2015; pp 297–301. https://doi.org/10.1109/RTSI.2015.7325114.

(48)   Balberg, I.; Binenbaum, N.; Anderson, C. H. Critical Behavior of the Two-Dimensional Sticks System. *Phys. Rev. Lett.* **1983**, *51* (18), 1605–1608. https://doi.org/10.1103/PhysRevLett.51.1605.

(49)   Venezian, G. On the Resistance between Two Points on a Grid. *Am. J. Phys.* **1994**, *62* (11), 1000–1004. https://doi.org/10.1119/1.17696.

(50)   Consortium 16NRM01 EMPIR GRACE. *Good Practice Guide on the Electrical Characterization of Graphene Using Non-Contact and High-Throughput Methods*; Fabricius, A., Cultrera, A., Catanzaro, A., Eds.; 2020.

(51)   Xu, L.; Yang, Y.; Hu, Z.-W.; Yu, S.-H. Comparison Study on the Stability of Copper Nanowires and Their Oxidation Kinetics in Gas and Liquid. *ACS Nano* **2016**, *10* (3), 3823–3834. https://doi.org/10.1021/acsnano.6b00704.

(52)   Elechiguerra, J. L.; Larios-Lopez, L.; Liu, C.; Garcia-Gutierrez, D.; Camacho-Bragado, A.; Yacaman, M. J. Corrosion at the Nanoscale: The Case of Silver Nanowires and Nanoparticles. *Chem. Mater.* **2005**, *17* (24), 6042–6052. https://doi.org/10.1021/cm051532n.

(53)   Eom, H.; Lee, J.; Pichitpajongkit, A.; Amjadi, M.; Jeong, J.-H.; Lee, E.; Lee, J.-Y.; Park, I.

Ag@Ni Core-Shell Nanowire Network for Robust Transparent Electrodes Against Oxidation and Sulfurization. *Small* **2014**, *10* (20), n/a-n/a. https://doi.org/10.1002/smll.201400992.

(54)   Jiu, J.; Wang, J.; Sugahara, T.; Nagao, S.; Nogi, M.; Koga, H.; Suganuma, K.; Hara, M.; Nakazawa, E.; Uchida, H. The Effect of Light and Humidity on the Stability of Silver Nanowire Transparent Electrodes. *RSC Adv.* **2015**, *5* (35), 27657–27664. https://doi.org/10.1039/C5RA02722E.

(55)   Moon, I. K.; Kim, J. Il; Lee, H.; Hur, K.; Kim, W. C.; Lee, H. 2D Graphene Oxide Nanosheets as an Adhesive Over-Coating Layer for Flexible Transparent Conductive Electrodes. *Sci. Rep.* **2013**, *3* (1), 1112. https://doi.org/10.1038/srep01112.

TABLE OF CONTENTS (TOC) GRAPHIC